Journal of Alloys and Compounds 899 (2022) 163266

Contents lists available at ScienceDirect

Journal of Alloys and Compounds

journal homepage: www.elsevier.com/locate/jalcom

Full length article

Thermal deformation behavior of GO/CeO_2 in-situ reinforced Cu30Cr10W electrical contact material

Shengli Liang[a,1], Meng Zhou[a,b,c,*,1], Yi Zhang[a,b,c,*], Shuang Liu[a,1], Xu Li[d], Baohong Tian[a,b,c], Yongfeng Geng[a,e], Yijie Ban[a,f], Yanlin Jia[g], Yong Liu[a,b,c], Alex A. Volinsky[h]

[a] School of Materials Science and Engineering, Henan University of Science and Technology, Luoyang 471023, China
[b] Provincial and Ministerial Co-construction of Collaborative Innovation Center for Non-ferrous Metal new Materials and Advanced Processing Technology, Luoyang 471023, Henan Province, China
[c] Henan Province Key Laboratory of Nonferrous Materials Science and Processing Technology, Luoyang 471023, China
[d] Center for Advanced Measurement Science, National Institute of Metrology, Beijing 100029, China
[e] State Key Laboratory of Metal Matrix Composites, Shanghai Jiao Tong University, Shanghai 200240, China
[f] College of Materials Science and Engineering, Huazhong University of Science and Technology, Wuhan 430074, China
[g] College of Materials Science and Engineering, Central South University, Changsha 410083, China
[h] Department of Mechanical Engineering, University of South Florida, Tampa 33620, USA

ARTICLE INFO

Article history:
Received 28 July 2021
Received in revised form 29 November 2021
Accepted 13 December 2021
Available online 15 December 2021

Keywords:
GO
In-situ formation of Cr_7C_3
Hot deformation
Constitutive equations
Microstructure evolution
Processing maps

ABSTRACT

Cu30Cr10W and GO/CeO_2-Cu30Cr10W composites were fabricated by the spark plasma sintering (SPS). The isothermal compression tests of the Cu30Cr10W and GO/CeO_2-Cu30Cr10W composites were carried out on the Gleeble-1500 thermo-mechanical simulator under the deformation temperatures of 600–900 °C and strain rates of 0.001–1 s^{-1}. The effects of graphene doped CeO_2 on the thermal deformation behavior and microstructure of the composites were investigated. The results show that a trace amount of Cr_7C_3 layers/nanoparticles was in-situ formed at the interface between graphene and metal matrix, and the interfacial adhesion of composites improved significantly. The Cr particles grew in strip shape perpendicular to the compression direction, and the edge of tungsten carbide particles deformed slightly. With the increased of deformation temperature from 700 ℃ to 900 ℃, the texture component changed to fiber texture. In addition, the constitutive equations of the three composites were obtained. Compared with Cu30Cr10W composites, the addition of GO/CeO_2 and the accompanying twinning mechanism increased the flow stress, and the activation energy increased by 8.4% and 33.1%, respectively. Furthermore, the hot working performance is obviously improved.

© 2021 Published by Elsevier B.V.

1. Introduction

Improving the performance of working parts under harsh conditions is the driving force for the development of new materials. In addition, with the in-depth development of the concept of energy conservation and environmental protection, a single material with different properties can meet the application in many fields, which makes the scientific research focus on composite materials [1,2]. Due to its high electrical conductivity and thermal conductivity, copper is a challenging candidate for high performance materials in thermal and electrical fields. In the past research, Al_2O_3 [3,4], SiC [5], WC [6], ZrB_2 [7] and TiB_2 [8] were usually used as the main reinforcing phases in copper matrix composites. Although the strength of the composite was greatly improved, the electrical conductivity was irreversibly sacrificed [9]. With the rapid development of modern industry and emerging science, higher requirements are put forward for the performance of conductor materials [10]. Breaking through the bottleneck of high strength and high conductivity is the inevitable trend of long-term development of copper matrix composites.

Graphene, the single-atom-thick sheet composed of sp2-hybridized carbons [11], it has been attracted as an unearthly reinforcing material for structural and functional applications due to its excellent mechanical, thermal and electrical properties [12–15], and

* Corresponding authors at: School of Materials Science and Engineering, Henan University of Science and Technology, Luoyang 471023, PR China
E-mail addresses: zhoumeng0902@126.com (M. Zhou), yizhang@huast.edu.cn (Y. Zhang).
[1] These authors contributed equally to this work.

https://doi.org/10.1016/j.jallcom.2021.163266
0925-8388/© 2021 Published by Elsevier B.V.

the results show that graphene had made a great contribution to the mechanical properties of metal matrix composites. For example, graphene oxide and surfactant were introduced into copper matrix by electrostatic self-assembly and powder metallurgy methods and the graphene-copper composites showed enhanced mechanical properties and thermal conductivity [16]. This is mainly due to the graphene has a series of excellent physical and chemical properties, such as excellent electron transport properties and large specific surface area (2630 m^2g^{-1}) [17]. Furthermore, Zhang et al. have reported that the strength and conductivity of graphene reinforced alumina Al_2O_3-CuWCr composites prepared by vacuum hot pressing sintering method were increased by 45% and 10% respectively, which was attributed to the uniform dispersion of graphene and the strong interfacial bonding between graphene and matrix [18]. However, little attention has been paid to the hot working behavior of graphene copper matrix composites.

Hot working is a part of the common heat treatment process for metal materials, which is widely used in manufacturing industry to improve the performance of various metal materials [19]. Hot deformation temperature and hot deformation strain rate play a leading role in the microstructure evolution and final properties of products [20]. Through macro-control and simulation of deformation parameters, the optimal deformation parameters can be obtained to improve the microstructure inhomogeneity and hot working cracking. In recent years, copper matrix composites are the key research and development materials in the field of electrical contact. Although widely investigated on the electrical conductivity, mechanical strength and arc erosion characteristics, there are few reports in the field of thermal deformation behavior. Hiraoka [21] et al. carried out compression tests on W-80vol% Cu composites at the room temperature, with the increased of strain rates, the fibrous structure gradually appeared in the inner grains.

Based on the above research, GO and CeO_2 were introduced into CuCrW composites by mechanical ball milling, freeze-drying and spark plasma sintering. On the one hand, GO has good wettability with metal matrix, and can be transformed into RGO during sintering. At the same time, the electrical and mechanical properties of graphene can be restored. Cerium dioxide, an environmentally friendly rare earth oxide, has appealed considerable attention on account of its low cost, good chemical stability and high ionic conductivity [22]. The effects both on electrical properties and mechanical strength have been reported in our previous work [23]. On the other hand, the electrical contact materials produce high temperature in the process of arc ablation. Moreover, the mechanical behavior and failure mechanism are very different from those at room temperature. Therefore, the deformation behavior of 0.5GO/0.5CeO_2-Cu30Cr10W and 1.0GO/0.5CeO_2-Cu30Cr10W composites were investigated by isothermal compression test on Gleeble-1500D thermal simulator with the deformation temperatures of 600–900 °C and strain rates of 0.001–1 s^{-1}. The microstructure evolution, electron backscatter diffraction (EBSD) images and TEM were analyzed during hot deformation. Finally, the influence of GO and CeO_2 on the flow stress and thermal deformation activation energy of the composites was determined.

2. Experimental materials and process

Raw materials mainly include the pure copper powder (3–5 μm diameter , purity > 99.95%), W powder and Cr powder (purity > 99.9%, average diameters 5 μm and 47 μm, respectively), CeO_2 powder (purity > 99.95%, particle size < 50 nm); Graphene oxide was prepared by modified Hummers method [24]. Table 1 shows the nominal composition of three composites. Pure copper ball was used as grinding medium, and mixed powder was milled in QM-3SP2 planetary mill with ball-powder weight ratio of 5:1 for 8 h to obtain composite powder. After freeze-drying, the composite powder was sintered in SPS furnace. The sintering parameters were vacuum degree of 6×10^{-2} Pa and heating rate of 100 °C/min. When the sample was ~~is~~ heated to 600 ℃, the axial pressure of 30 MPa was applied and kept for 3 min, the final sintering temperature is 900 °C and kept for 5 min, then dropping the temperature to below 100 °C prior to sample removal.

Table 1
The nominal composition of the composites.

Materials	Analyzed composition (wt%)				
	Cr	W	GO	CeO_2	Cu
Cu30Cr10W	30	10	–	–	Bal.
0.5GO/0.5CeO_2-Cu30Cr10W	30	10	0.5	0.5	Bal.
1.0GO/0.5CeO_2-Cu30Cr10W	30	10	1.0	0.5	Bal.

The relative density, conductivity and Vickers hardness of the as sintered samples were measured , and the microstructure evolution were analyzed by the JSM-7800 field emission scanning electron microscope and JEM-2100 transmission electron microscope. As-sintered composites were cut into the size for Φ8 mm× 12 mm cylindrical hot compression specimens by wire EDM. Isothermal axial compression test was performed using the Gleeble-1500d thermal simulation testing machine. Raising the temperature to the set deformation temperature at the heating rate of 10 °C/min, the deformation temperature were 600 °C, 700 °C, 800 °C and 900 °C, and the deformation rates were 0.001 s^{-1}, 0.01 s^{-1}, 0.1 s^{-1} and 1 s^{-1}, respectively. To ensure the integrity of high temperature structure, water quench was immediately needed after hot deformation. In order to analyze the microstructure evolution during thermal deformation, samples were taken along the section perpendicular to the stress direction, and then polished, etched and observed by the optical microscope (OM). In addition, thin sections with a diameter of 3 mm and a thickness of below 100 μm were ion thinned. After removal, EBSD images were obtained using JSM-7800 field emission scanning electron microscope. Moreover, the samples can be used for EBSD tests using JEM-2100 transmission electron microscope.

3. Result and discussion

3.1. True stress-true strain curves

In the process of hot deformation, the change of true stress-strain curve is comprehensively effected by the work hardening, dynamic recovery and dynamic recrystallization [25,26]. Under the condition of constant temperature or strain rate, the flow stress shows different trends. Flow stress increases rapidly at the initial stage of hot deformation and reaches the peak stress. It can be considered that in the initial stage of deformation, with the generation of a large number of slip dislocations at the grain boundary and stress concentration, the dislocation density in the deformation area rises sharply, and the dislocation entanglement forms a barrier for dislocation movement, which increases the resistance of dislocation movement and shows the obvious characteristics of work hardening. Over time, strong atomic thermal motion will consume the resistance of dislocation motion [27–29]. Therefore, the flow stress will gradually decrease and tend to be stable. In general, the process mainly experienced dynamic recrystallization and dynamic recovery. The cross slip and climb of dislocations play an important role in dynamic recovery, which included the reverse dislocation neutralization, dislocation rearrangement and reduction of dislocation density. In addition, dynamic recrystallization can eliminate dislocations and sub grain boundaries in the deformed matrix [30,31]. Therefore, the change trend of flow stress depends on the dynamic relationship between work hardening, dynamic recovery and dynamic recrystallization, which is macroscopically affected by deformation temperature and strain rate.

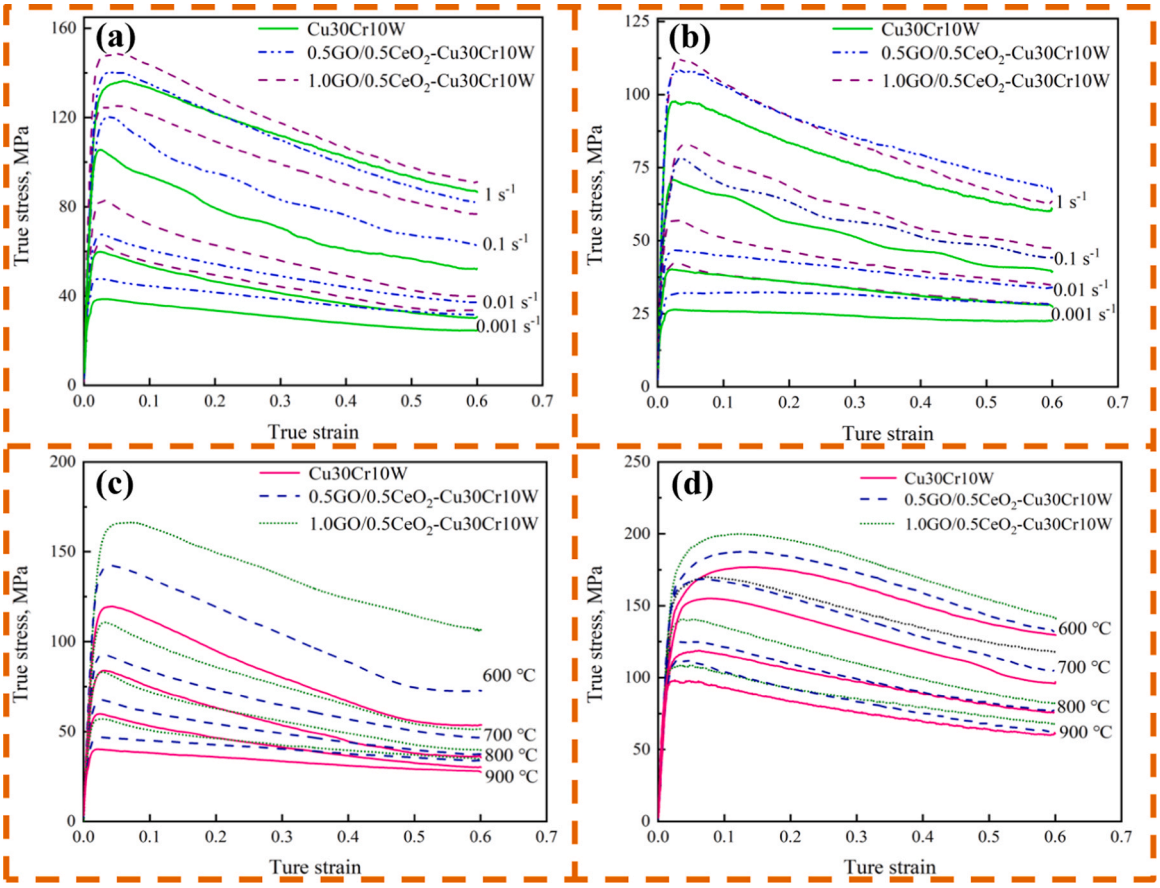

Fig. 1. True stress-true strain curves of Cu30Cr10W, 0.5GO/0.5CeO_2-Cu30Cr10W and 1.0GO/0.5CeO_2-Cu30Cr10W composite: (a)T = 800 ℃, (b)T = 900 ℃, (c) $\dot{\varepsilon}$ = 0.01 s^{-1}, (d) $\dot{\varepsilon}$ = 1 s^{-1}.

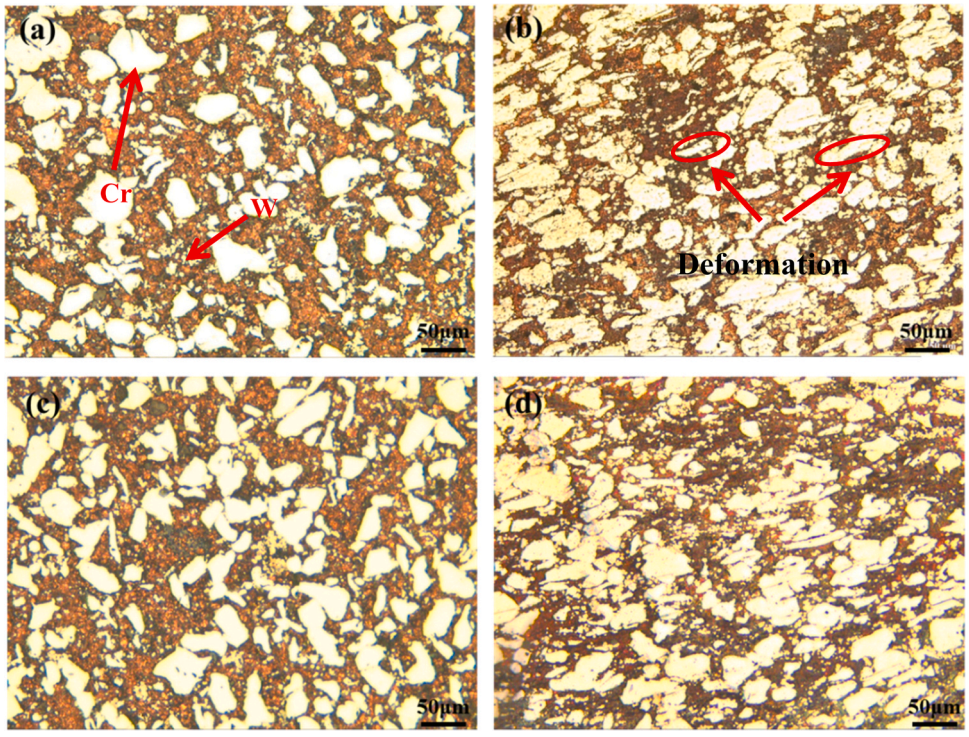

Fig. 2. Optical microscope image of the two composites at different conditions: (a) As-sintered 0.5GO/0.5CeO_2–Cu30Cr10W; (b) 0.5GO/0.5CeO_2–Cu30Cr10W deformed at 900 °C, 0.1 s^{-1}; (c) As-sintered 1.0GO/0.5CeO_2–Cu30Cr10W; (d) 1.0GO/0.5CeO_2–Cu30Cr10W deformed at 900 °C, 0.1 s^{-1}.

Fig. 1 shows the true stress-strain curves of the three composites at 800 °C, 900 °C, 0.01 s^{-1} and 1 s^{-1}, respectively. Fig. 1(a) and (b) illustrate the flow stress of the three composites at 800 °C and 900 °C. The results show that the flow stress of the same material increased with the increase of strain rate. For example, at 800 °C, the peak flow stress of 1.0 GO/0.5CeO_2-Cu30Cr10W at 0.01 s^{-1} and 1 s^{-1} strain rates was 84 MPa and 156 MPa, respectively. The reason is that dynamic recrystallization was easier to occur at low strain rates. In addition, at low strain rate, the flow stress reached the peak and then tended to be stable. Fig. 1(c) and (d) show the flow stress curves of the three composites at 0.01 s^{-1} and 1 s^{-1} strain rates, respectively. The curves show that the peak value of flow stress of the same material decreased with the increase of strain temperature at the same strain rate. It can be seen that when the strain rate was 1 s^{-1}, the peak flow stress of 1.0GO/0.5CeO_2-Cu30Cr10W at 600 °C and 900 °C was 203 MPa and 119 MPa respectively, which can be explained by the fact that dynamic recrystallization was easier to occur at high temperature. In addition, the true stress-strain curve at higher deformation temperature reached peak and became flat gradually.

Compared with the flow stress of Cu30Cr10W composite, the maximum flow stress of GO/CeO_2-Cu30Cr10W composite was always in the leading position under the same hot deformation conditions, which was the result of the combined action of graphene and rare earth elements. On the one hand, the large difference of thermal expansion coefficient between graphene and copper matrix led to high density dislocations at grain boundaries [18]. On the other hand, rare earth elements can refine the grain, which can strengthen the fine grain, and improve the mechanical strength and plastic toughness of the material. CeO_2 nanoparticles can hinder the movement of dislocation and grain boundary. Finally, the flow stress of GO/CeO_2-Cu30Cr10W composite increased significantly [26,32].

3.2. Microstructure

Fig. 2 shows the microstructure of the two composites before and after thermal deformation under optical microscope. It can be seen from Fig. 2(a) and (c) that the sintered composite had compact structure without obvious holes and other macroscopic defects. There was no obvious agglomeration of W and Cr particles on the copper matrix. Fig. 2(b) and (d) show the microstructure of the two composites after deformation at 900 ℃ and 0.1 s^{-1}, respectively. Compared with the sintered state, after deformation, some of the Cr particles became strips and elongated along the direction perpendicular to the deformation direction. Due to the characteristics of high hardness and high melting point of W, the morphology change was not obvious during hot deformation.

In the process of hot deformation, the microstructure was subjected to the combined action of compressive stress and tensile stress in different directions, and micro defects were more likely to occur at the interface junction, resulting in the degradation of properties and eventually the overall failure of the material. Strong interface was an essential requirement to ensure the effective load transfer of graphene metal matrix composites in the process of preparation and processing [33]. Fig. 3 shows the interface structure and interface relationship between graphene and matrix. It can be seen from Fig. 3(a) that there were spherical and island shaped small-size nanoparticles at the interface. Through the selective area diffraction patterns (SADPs) of A_1 and A_2 regions, the diffraction spots as shown in Fig. 3(c) can be obtained. It can be proved that the small-size nanoparticles were Cr_7C_3 with the hexagonal structure, and the lattice parameters are a= 13.98 nm, b= 13.98 nm, c= 4.523 nm, and $\alpha = \beta = \gamma = 90^\circ$. Moreover, the zone axis of copper matrix and Cr_7C_3 are $[0\bar{1}\bar{1}]$ and [010], respectively. As illustrated in Fig. 3(c), it can be clearly seen that the $(\bar{1}\bar{1}1)$ plane of copper is not parallel to the (600) crystal plane of Cr_7C_3, but has a phase difference of 4.08° . Fig. 3(b) and (d) were the selected area electron diffraction patterns of A_3 region respectively, which can confirm the existence of graphene and CeO_2. Moreover, CeO_2 was uniformly distributed on graphene, and there was no large area agglomeration phenomenon.

According to the research of Anthonysamy and Teng [34,35], there are three chemical reactions in C-Cr system:

$$3Cr + 2C = Cr_3C_2,\ \Delta G = -58857 - 22.34T \quad (1)$$

$$7Cr + 3C = Cr_7C_3,\ \Delta G = -92067 - 41.5T \quad (2)$$

$$23Cr + 6C = Cr_{23}C_6,\ \Delta G = -236331 - 86.2T \quad (3)$$

Where T is the actual reaction temperature (K) and ΔG is the Gibbs free energy (J/mol). At present, the sintering temperature of SPS is 900 ℃ (1173.15 K), and the ΔG of three carbon chromium compounds are − 85.07KJ/mol, − 140.75 KJ/mol and − 337.46 KJ/mol, respectively. It can be seen that the lowest ΔG is required to generate $Cr_{23}C_6$, but there is no relevant research to prove its existence in C-Cr system. Compared with Cr_3C_2, the formation of Cr_7C_3 is easier from a thermodynamic point of view [33]. However, in our previous research, Cr_3C_2 was found at the rGO/Cu interface, and Cr_7C_3 was found after isothermal compression test. This is an interesting phenomenon. At present, this is not well understood, but we will continue to explore it in the next research.

Based on the above TEM images and analysis, the possible formation mechanism of rGO and Cr_7C_3 nanoparticles was simulated. With the progress of high-temperature sintering process, GO loses oxygen-containing functional groups and the content of oxygen-free carbon increases significantly, which has been proved in our previous research. At the same time, high current and large Joule heat will cause slight damage to the surface of graphene, form a small amount of amorphous carbon atoms and gather into the activated carbon layer (ACL), Cr atoms diffuse to ACL and reach a certain atomic concentration, and the absorption effect will occur to form Cr_7C_3 core, as shown in Fig. (e_1) and (e_2). The Cr_7C_3 nucleus continues to grow until all activated carbon atoms are exhausted. This process is cyclic, the newly formed amorphous carbon atoms builds a bridge for the fusion of adjacent Cr_7C_3 nuclei and gradually forms Cr_7C_3 particles, as shown in Fig. (e_3).

Geometric Phase Analysis (GPA) is an effective image processing technology, which is very sensitive to small strains in high-resolution TEM (HR-TEM) images. Fig. 4(a) shows a representative HR-TEM image of the impurity free interface between rGO/CeO_2 and copper matrix. Fig. 4(b) and (c) confirm the substances on both sides of the interface, and high-density dislocations are found in the copper matrix along the Cu$[0\bar{1}1]$ zone axis. The corresponding FFT was also shown in upper right inset of Fig. 4(b). Fig. 4(d) is the GPA corresponding to Fig. 4(a), and the color map represents the positive strain according to the ε_{xx} [111] direction. From the color reaction, most of rGO and CeO_2 show homogeneous strain, but the copper matrix shows the opposite situation, showing a large strain difference. The results show that there is a stronger interaction for dislocations during deformation, and the lattice distortion effect of rGO and matrix plays an important role in strengthening graphene/copper matrix composites.

Fig. 5 shows the evolution of microstructure during hot deformation. In the process of isothermal compression, due to the effect of work hardening, driven by stress and temperature, dislocations slide at the stress concentration such as grain boundary, resulting in a large number of entanglements, forming clear deformation bands and a large number of dislocation packets, as shown in Fig. 5(a) and (b). In addition, the edge of the tungsten particles is slightly deformed, as shown in Fig. 5(c). The reason is that the tungsten particles have high hardness, and the dislocation was blocked in the process of movement and accumulated around the tungsten particles, resulting in the phenomenon of stress concentration. It can be seen from Fig. 5(d) that a large number of

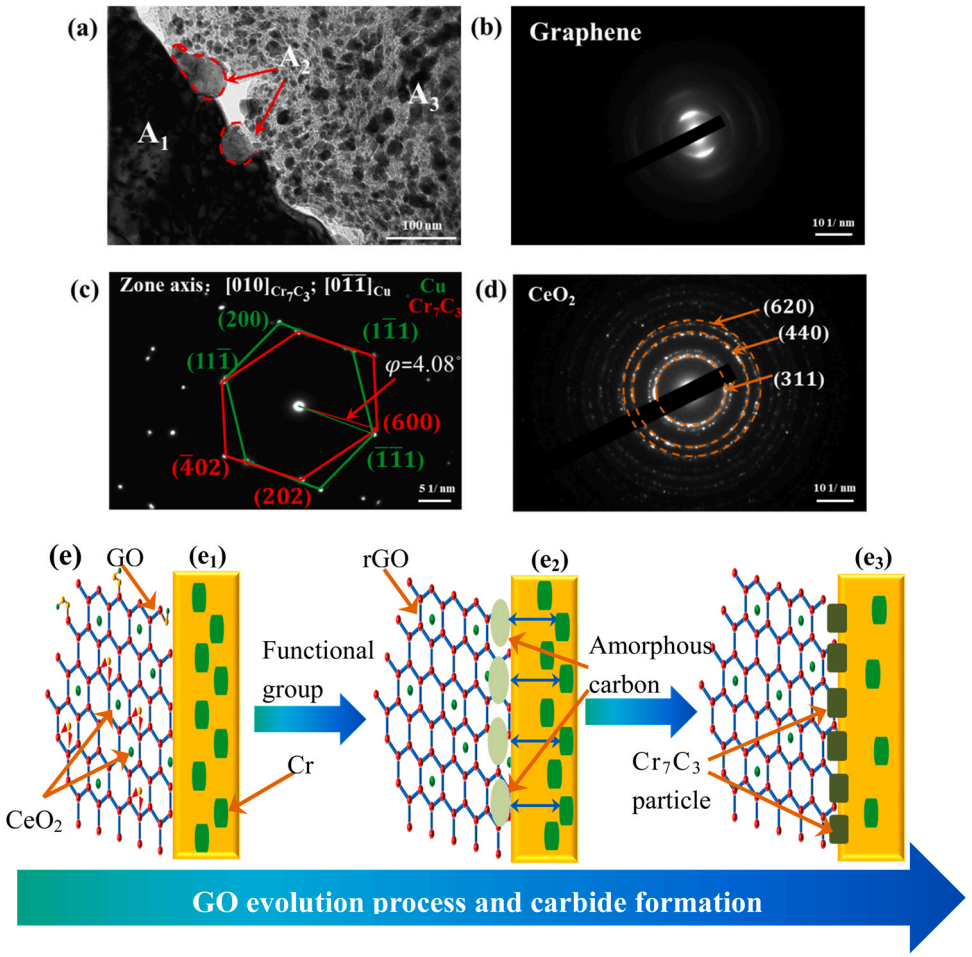

Fig. 3. (a) TEM images of the interface between graphene and matrix in the composite; (b) and (d) A_3 region selective electron diffraction; (c) Selective electron diffraction in A_1 and A_2 regions;(e) GO evolution process and carbide formation.

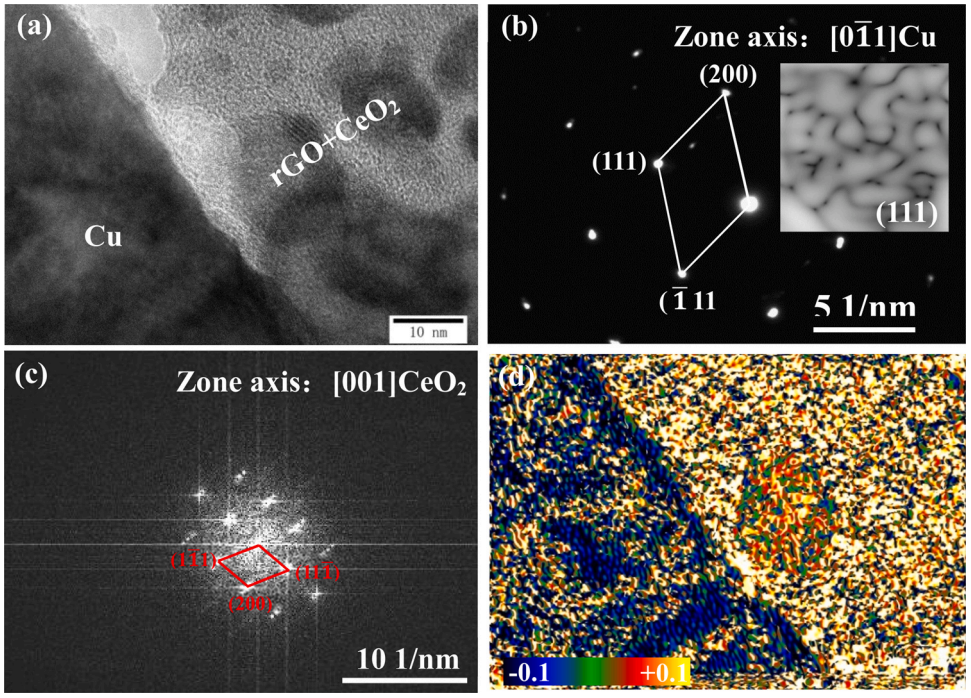

Fig. 4. Analyses on rGO/CeO_2-Cu interfaces. (a)TEM micrograph image showing the rGO/CeO_2-Cu interface, (b and c) FFT of Cu and CeO_2, (d) GPA map of the (a).

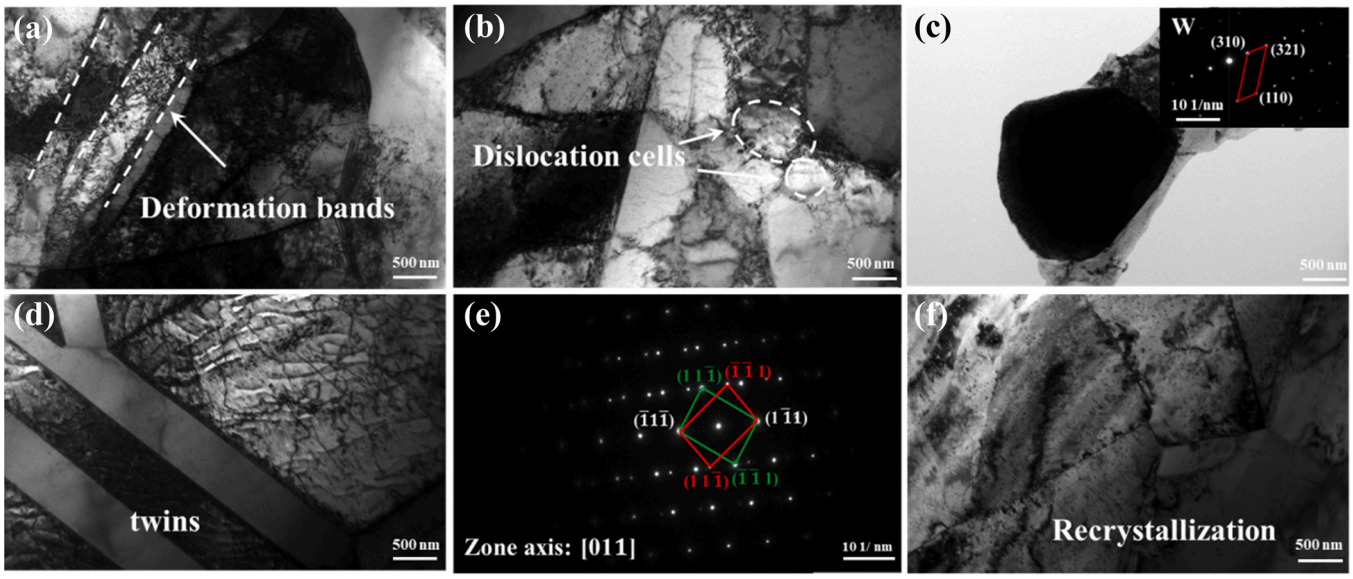

Fig. 5. TEM microstructure of: (a) and (b) deformation bands and dislocation packets; (c) Deformed W particles; (d) and (e) twins; (f) Deformed structure.

dislocation lines around the twins are entangled and interweaved into a network structure. The selected area electron diffraction image in Fig. 5(e) can determine that the zone axis of the twins is [011]. Fig. 5(f) shows that the material has recrystallized.

Compared with Cu30Cr10W composites, Cr_7C_3 nanoparticles with small size were formed at the interface between amorphous carbon atoms and Cr particles, which optimized the interface between graphene and metal matrix and reduced the occurrence probability of interface defects during hot deformation. In addition, the plastic deformation of metals is controlled by both slip and twinning. Owing to the difference of thermal expansion coefficient between graphene and metal matrix, the movement of dislocations is hindered. When dislocation entanglement leads to slippage, twins play an important role. In the process of preferred growth, some atoms are transferred from the orbit which is not conducive to slip to the position which is conducive to slip, which completely changes the orientation of the crystal and further promotes the process of slip and crystal deformation. In addition, twin boundaries promote more grain boundary growth and have pinning effect on grain boundary migrations. According to the above analysis, we can explain why the addition of graphene can improve the flow stress and activation energy.

3.3. EBSD analysis

The main research directions of EBSD are the measurement of grain orientation, orientation difference, analysis of real grain size and texture evolution [36,37]. In order to investigate the texture evolution, grain size and misorientation angle of GO/CeO_2-Cu30Cr10W composites after isothermal compression test, EBSD data were obtained by JSM-7800 F back scattering scanning electron microscope. Fig. 6 shows EBSD images of GO/CeO_2-Cu30Cr10W composites under isothermal compression at 700 ℃, 0.01 s^{-1} and 900 ℃, 0.01 s^{-1}, respectively. As shown in Fig. 6(a) and (c), the grains were seriously deformed after isothermal compression test, and recrystallized grains were distributed around the deformed grains. With the increase of deformation temperature, the fine recrystallization grains gradually disappeared, and the deformed grains were replaced by the growing recrystallization grains. Thus, the increased of temperature provided the power for dynamic recrystallization and promoted the growth of the grains. As shown in Fig. 6(b) and (d), it can be seen that the overall trend of error angle distribution was same, and the concentrations of low error angle and high error angle were approximately equal. When the deformation temperature was low, there were a lot of deformed grains and low angle grain boundaries (LAGBs, misourintation angle < 15°), as shown in Fig. 6(b), which resulting in a large number of dislocations gathering in deformed grain boundaries and processing hardening areas. With the increased of deformation temperature, the content of HAGBs increased from 46.3% to 56.6%, which was as result of that increased of temperature enhanced the recrystallization trend, promoted the growth of dynamic recrystallized grains, and caused a large number of dislocations to be swallowed up. Moreover, the increased of temperature driven the LAGBs to change into HAGBs with the rotation of sub grain [20]. This shows that the increased of large angle grain boundaries represented the enhancement of dynamic recrystallization and the decrease of dislocation density.

Grain boundary migration plays an important role in the process of thermal deformation. The migration rate of grain boundary is closely related to the dislocation density around the grain boundary. The Kernel Average Misorientation (KAM) obtained by EBSD can be used to judge the stress distribution state of composites during deformation. Therefore, exploring of dislocation density near grain boundary is of great significance to GO/CeO_2 reinforced Cu30Cr10W composites. The relationship between geometrically necessary dislocation (GND) density and (KAM) is as follows [38,39]:

$$\rho^{GND} = 2\theta/\mu b \tag{4}$$

Where ρ^{GND} represents the geometrically necessary dislocation density (m^{-2}), θ is the average local misorientation (rad), which is defined the critical value of the average local misorientation as 3°. μ is the scan step and b is the Burger's vector (2.55 nm) [28].

Fig. 7 shows KAM of 0.5GO/0.5CeO_2-Cu30Cr10W composite at deformation rate of 0.01 s^{-1} and different temperatures of 700 ℃ and 900 ℃, respectively. It can be seen that the GND is 1.42×10^{15} m^{-2} and 1.2×10^{15} m^{-2}, respectively in Fig. 7(a-b). The results show that the value of GND decreases with the increase of temperature, which proves that the generation of DRX consumes dislocations.

In order to investigate the texture evolution under different thermal deformation conditions, the polar and inverse polar figures of the composites with low crystal indexes of {110}, {100} and {111} were observed at 700 ℃, 0.01 s^{-1} and 900 ℃, 0.01 s^{-1}, respectively, as shown in Fig. 8. It can be seen from Fig. 8(a_1) and (b_1), the maximum texture strength under the deformation condition of 700 ℃, 0.01 s^{-1}

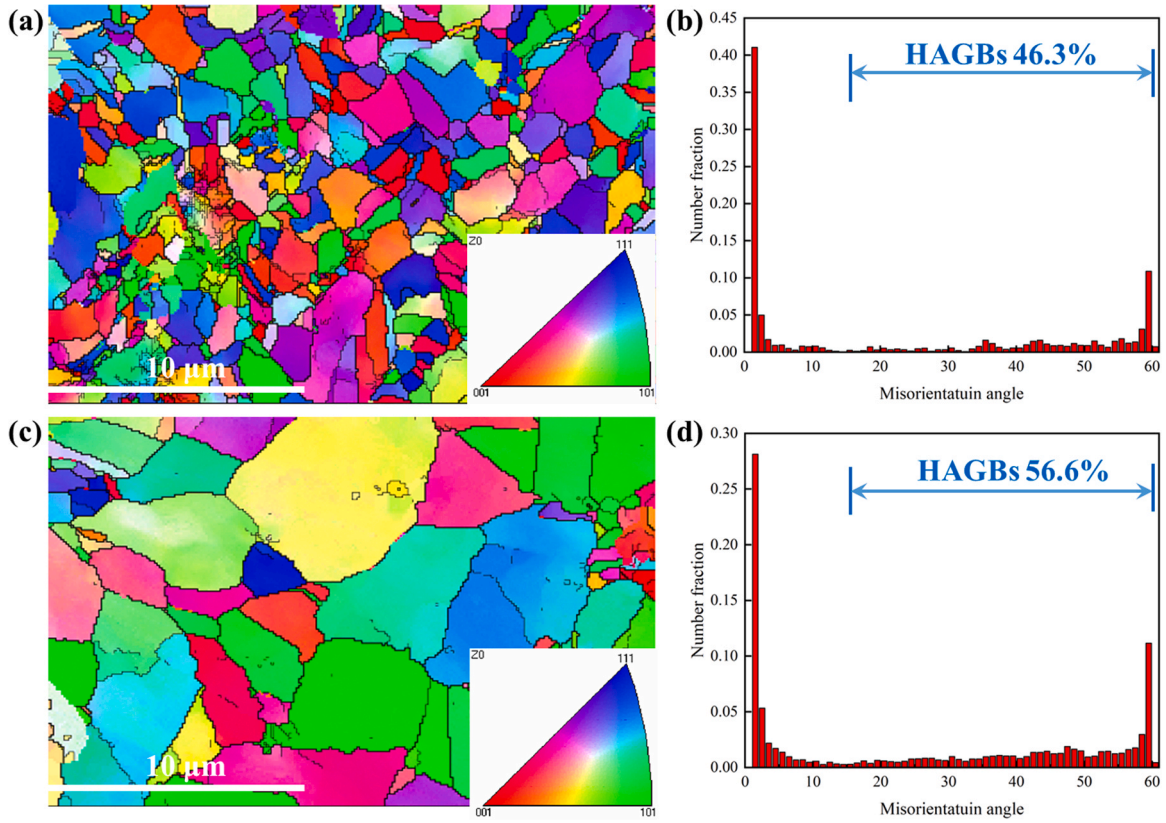

Fig. 6. EBSD images and misorientation angles distributions of 0.5GO/0.5CeO_2-Cu30Cr10W composites under different deformation conditions: (a) and (b) 700 ℃ , 0.01 s^{-1}; (c) and (d) 900 ℃ , 0.01 s^{-1}.

is 3.43. With the increased of deformation temperature, the maximum texture strength increased sharply to 8.75. In addition, we calculated the volume fraction of different textures, as shown in Fig. 8(c). At lower deformation temperature, the volume fraction for the ideal texture components of {011}< 100 >Goss texture, {011}< 112 >Brass texture, {112}< 111 >copper texture, S texture, < 100 > //X < 110 > //X and < 111 > //X were 4.29%, 11%, 5.52%, 12.7%, 17.2%, 37.6% and 17.5%, respectively. At higher deformation temperature, the corresponding volume fractions of ideal texture components were 0.64%, 10.4%, 3.32%, 5.24%, 10.1%, 53.4% and 25.4%, respectively. It can be observed that with the increase of temperature, the volume fraction of main textures, including Goss texture, Brass texture, Copper texture and S texture decreased and transformed into the fiber texture. Combined with the analysis of true stress-strain curve and microstructure evolution, the main texture is replaced by fiber texture, which mainly depends on the influence of dynamic recrystallization effect. According to the research results of Geng et al. [40], the reduction of volume fraction of main textures such as Goss texture and copy texture may lead to the reduction of mechanical properties and conductivity of composites.

3.4. Constitutive equation

There is a special mathematical relationship among temperature, strain rate and flow stress, which can be described by Arrhenius equation. At the same time, the Zener-Hollomon parameter (Z) is used to study the effects of strain rate and temperature on deformation behavior and DRX effect [41,42]. In addition, the activation energy of thermal deformation can be calculated, which can be used as the theoretical basis for judging the hot workability. Based on the true stress-strain curve, the constitutive equations of three kinds of composites are established. The parameter Z represents the lattice self-diffusion energy due to dislocation slip and climb.

$$Z = \dot{\varepsilon} \exp [Q/RT] \quad (5)$$

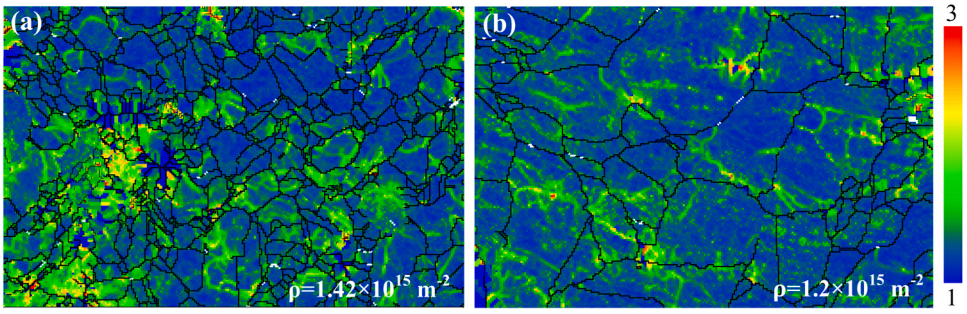

Fig. 7. The KAM of 0.5GO/0.5CeO_2-Cu30Cr10W composites under different deformation conditions: (a) 700 ℃ , 0.01 s^{-1}; (b) 900 ℃ , 0.01 s^{-1}.

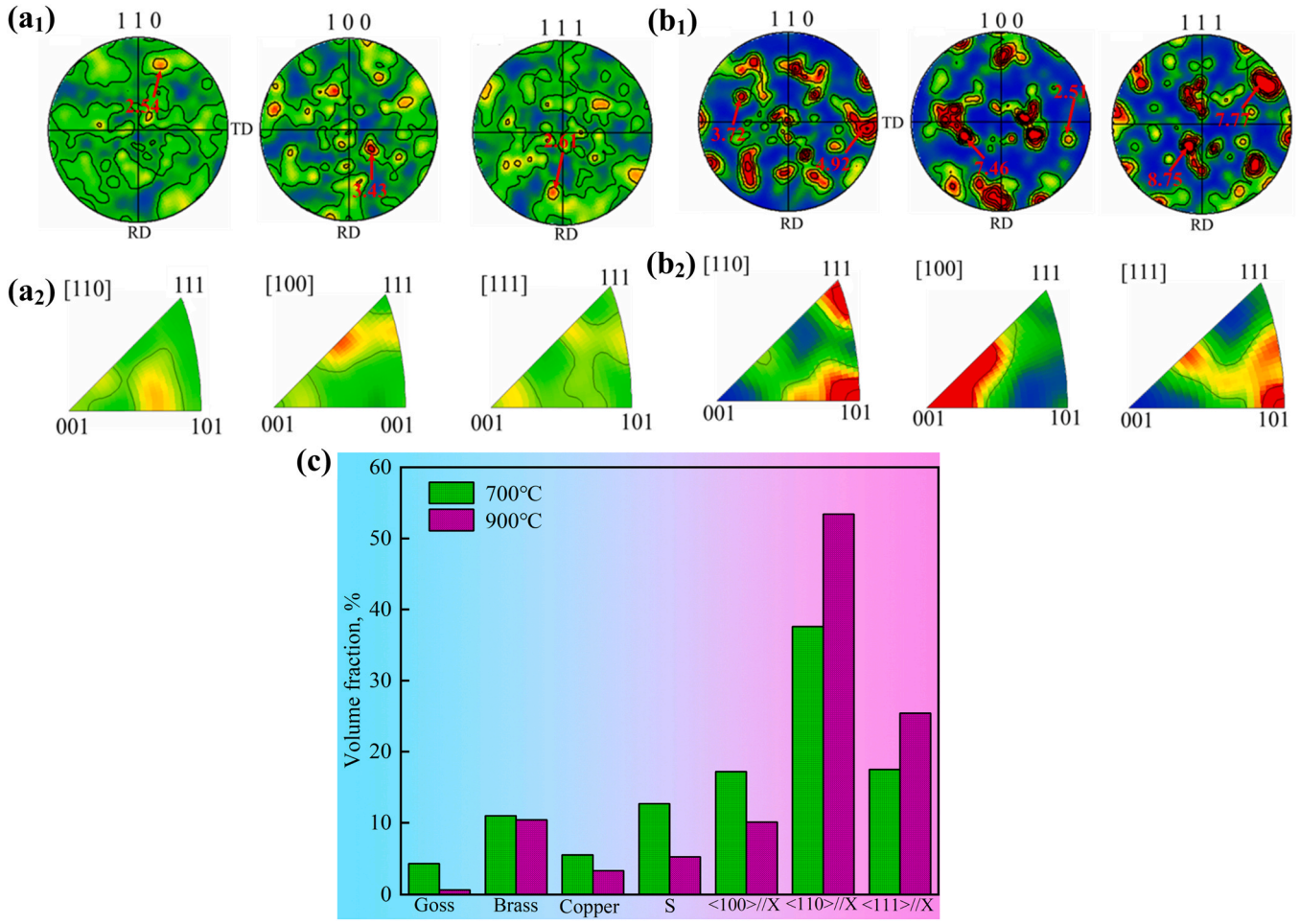

Fig. 8. Polar figures, inverse polefigures and texture volume fraction of 0.5GO/0.5CeO_2-Cu30Cr10W composites under different deformation conditions: (a_1) and (a_2) 700 ℃ , 0.01 s^{-1}; (b_1) and (b_2) 900 ℃ , 0.01 s^{-1} ; (c) Volume fraction of texture of different components.

Sellars and Mctegart [43] have proposed the hyperbolic sine model that gives better approximations between Zener–Hollomon parameter and flow stress. The description is as follows:

$$\dot{\varepsilon} = AF(\sigma)\exp(-Q/RT) \tag{6}$$

According to the value range of strain rate, Eq. (6) can be expressed as follows:

$$\dot{\varepsilon} = \begin{cases} A_1\,\sigma^{n_1}\exp[-Q/RT] & F(\sigma) = \sigma^{n_1} \quad (\alpha\sigma < 0.8) \\ A_2\exp(\beta\sigma)\exp[-Q/RT] & F(\sigma) = \exp(\beta\alpha) \quad (\alpha\sigma > 1.2) \\ A[\sinh(\alpha\sigma)^n]\exp[-Q/RT] & F(\sigma) = \sinh[\alpha\sigma]^n \quad (for \quad all) \end{cases} \tag{7}$$

Where A, $A1$, $A2$, α, β, n, n_1 and R is the constants, $\dot{\varepsilon}$ is the strain rate, T represents the thermal deformation temperature in K, R is the universal gas constant (8.314 J/mol/K), Q is the thermal deformation activation energy(J/mol), and σ is the flow stress. In Eq. (7), the power function equation is suitable for low-stress level ($\alpha\sigma < 0.8$), and the exponential equation is more suitable for high-stress level ($\alpha\sigma > 1.2$). In addition, the hyperbolic sine function model is compatible with all stress conditions [44,45].

Take the natural logarithm of the function in Eq. (7), respectively:

$$\ln\dot{\varepsilon} = \begin{cases} n_1\ln\sigma + \ln A_1 - Q/RTF(\sigma) = \sigma^{n_1}(\alpha\sigma < 0.8) \\ \beta\alpha + \ln A_2 - Q/RTF(\sigma) = \exp(\beta\alpha)(\alpha\sigma > 1.2) \\ n\ln[\sin h(\alpha\sigma)] - Q/RT + \ln AF(\sigma) = \sinh[\alpha\sigma]^n (for\ all) \end{cases} \tag{8}$$

The partial derivative of the hyperbolic sine model in Eq. (7) with respect to $\frac{1}{T}$ is calculated, and the expression of the activation energy of thermal deformation is obtained :

$$Q = R\left[\frac{\partial\ln\dot{\varepsilon}}{\partial\ln[\sin h(\alpha\sigma)]}\right]_T\left[\frac{\partial\ln[\sin h(\alpha\sigma)]}{\partial(1/T)}\right] = RnS \tag{9}$$

In this work, the thermal deformation activation energy of 1.0GO/0.5CeO_2-Cu30Cr10W is calculated as an example. Fig. 9 shows the relationships between deformation temperature, strain rate and peak flow stress of the 1.0GO/0.5CeO_2-Cu30Cr10W composite. Fig. 9(a-d) represent the relationship between $\ln(strain\ rate)$ and $\ln\sigma$, $\ln(strain\ rate)$ and σ, $\ln(strain\ rate)$ and $\ln[\sinh(\alpha\sigma)]$, $\ln(strain\ rate)$ and $1000/T$, respectively. Here, the values of material constants n_1, β, n and S are determined by average slope of the curve in Fig. 9(a-d). Thus, the values of n_1, β, n, and S are 10.28, 0.09, 7.49 and 3.98, therefore, the $\alpha = \beta/n_n = 0.009$. The thermal deformation activation energy of the 1.0GO/0.5CeO_2-Cu30Cr10W composite can be calculated as 247.9 KJ/mol from Eq. (9).

The hyperbolic sine model is introduced into Eq. (5) and the natural logarithm is taken as follows:

$$\ln Z = \ln A + n[\ln\sin h(\alpha\sigma)] \tag{10}$$

Fig. 9(e) shows the linear relationship between $\ln Z$ and $\ln[\sinh(\alpha\sigma)]$. Where $\ln A$ is the intercept of Fig. 9(e). Therefore, the value of A is $e^{25.16}$. According to the above values, the constitutive equations for the1.0GO/0.5CeO_2-Cu30Cr10W composite can be expressed as follows:

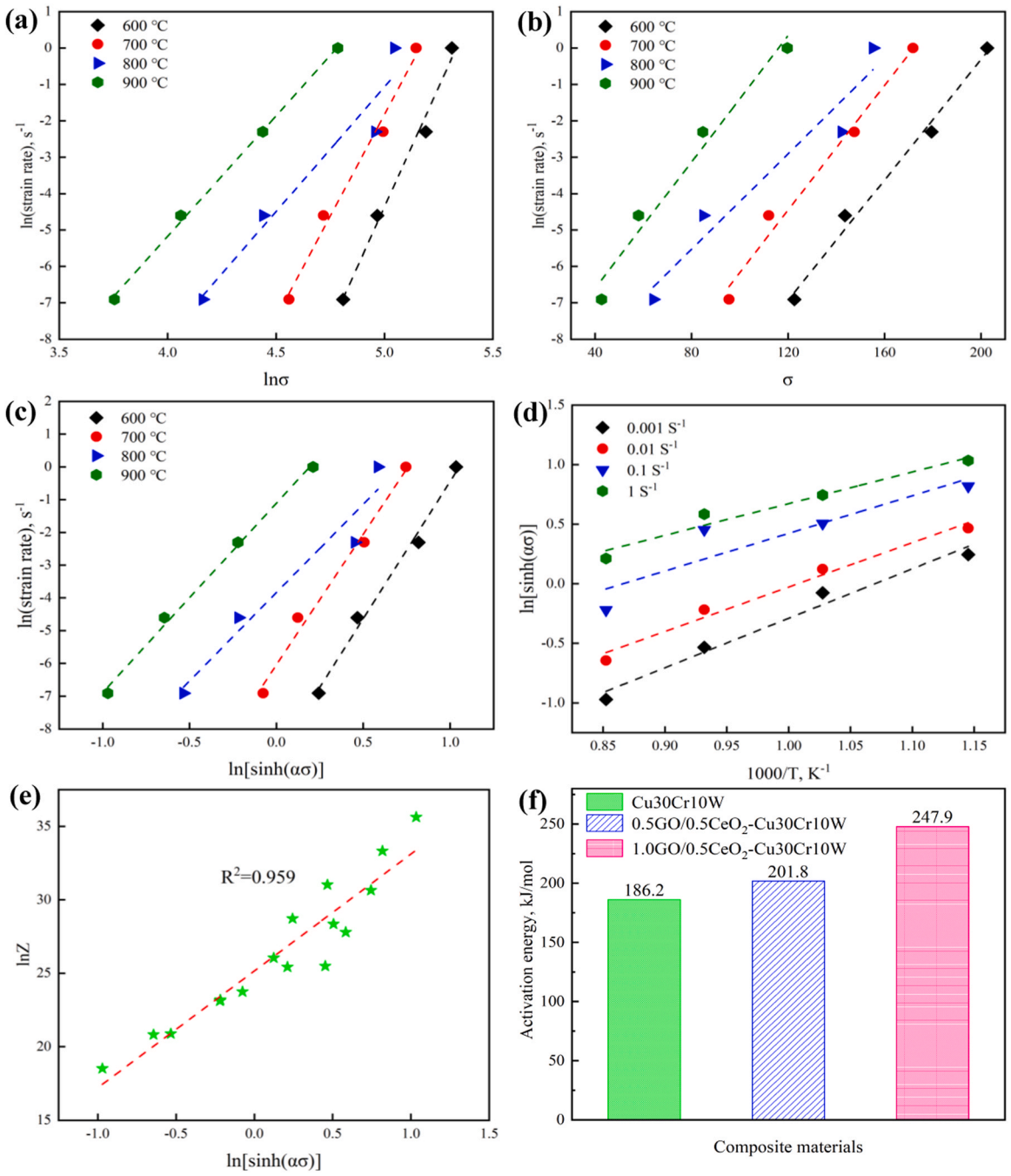

Fig. 9. Relations between: (a)ln(*strain rate*) − lnσ, (b)ln(*steain rate*) − σ, (c)ln(*strain rate*) − ln[sinh (ασ)], (d)ln[sinh(ασ)] − 1000/*T*, (e)ln*Z* − ln[sinh (ασ)], (f) activation energy of the Cu30Cr10W, 0.5GO/0.5CeO_2-Cu30Cr10W and 1.0GO/0.5CeO_2-Cu30Cr10W.

$$\dot{\varepsilon} = e^{25.16}[\sin h\,(0.009\sigma)]^{7.49} \exp\,(-247900/8.314T) \quad (11)$$

In the same way, we can obtain the constitutive equation of Cu30Cr10W and 0.5GO/0.5CeO_2-Cu30Cr10W composites as follows:

For the Cu30Cr10W composite:

$$\dot{\varepsilon} = e^{13.09}[\sin h\,(0.028\sigma)]^{2.81} \exp\,(-186200/8.314T) \quad (12)$$

For the 0.5GO/0.5CeO_2-Cu30Cr10W composite:

$$\dot{\varepsilon} = e^{18.71}[\sin h\,(0.013\sigma)]^{5.8} \exp\,(-201800/8.314T) \quad (13)$$

Fig. 9(f) shows the deformation activation energy of Cu30Cr10W, 0.5GO/0.5CeO_2-Cu30Cr10W and 1.0GO/0.5CeO_2-Cu30Cr10W. Compared with Cu30Cr10W, the thermal deformation activation energy of the other two composites increased by 8.4% and 33.1%, respectively, which indicated that the introduction of GO and CeO_2 improved the high temperature stability of the composites. The reason may be the load redistribution effect caused by graphene [46], and the coefficient of thermal expansion between graphene and matrix is very different. In the process of thermal deformation, the movement of dislocations at the interface between graphene and matrix is hindered. Moreover, the addition of graphene hinders the diffusion of copper atoms, leading to the grain refinement of the composite, so as to achieve the effect of fine grain strengthening [47,48]. Another reason is that CeO_2 nanoparticles restrict the movement of dislocations.

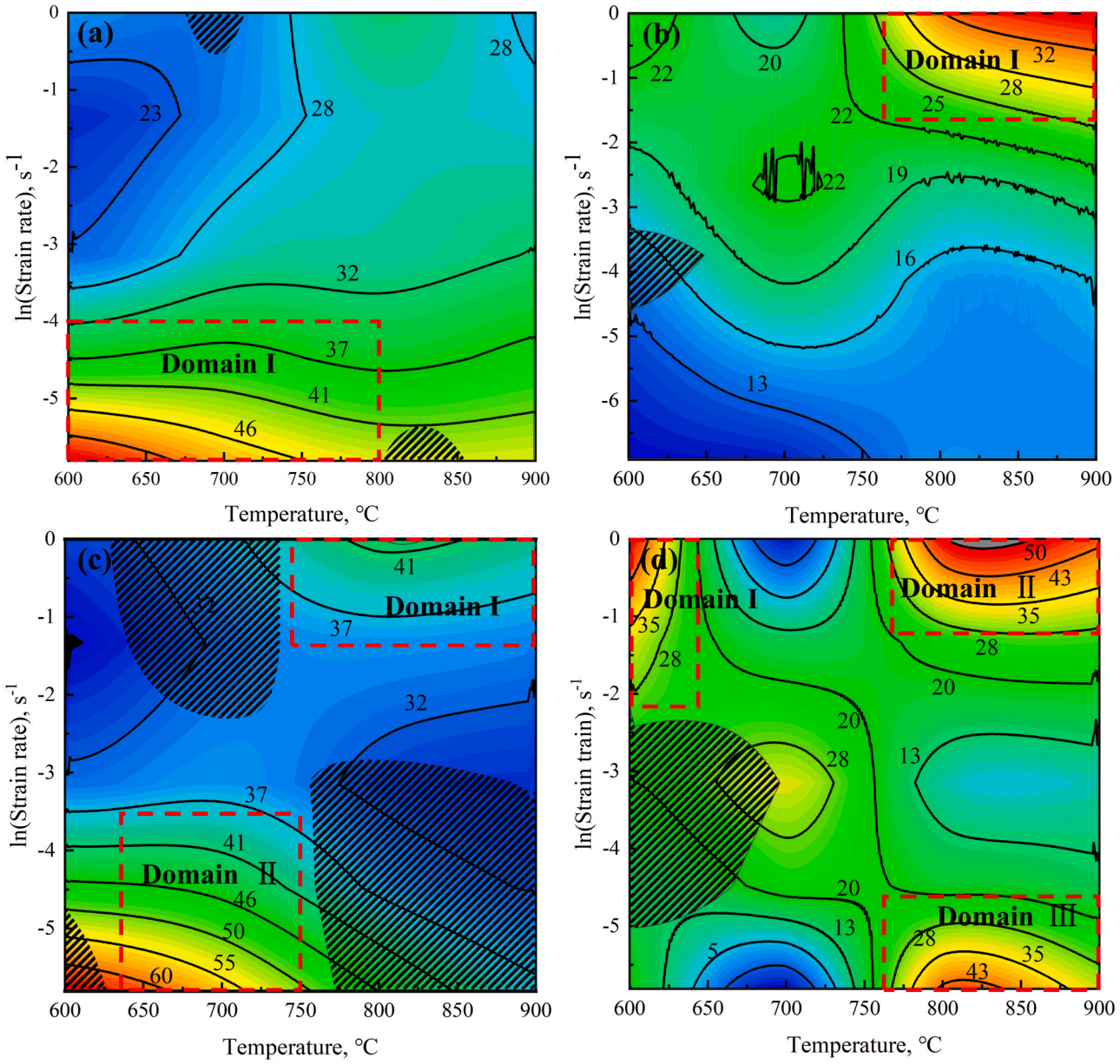

Fig. 10. Processing map of the Cu30Cr10W and 1.0GO/0.5CeO_2-Cu30Cr10W composite deformed at the strain of 0.2 (a) and (b); 0.4 (c) and (d).

3.5. Processing map analysis

In order to further evaluate the response of microstructure evolution of composites to thermal processing parameters during hot working and provide the basis for parameter optimization, the processing maps were established based on the dynamic material model. In the process of thermal deformation, the material itself is considered as a power dissipator. The microstructure transformation of the workpiece can be reflected by the power dissipation diagram [29], and the power dissipation efficiency (η), which can be defined as Eq. (14):

$$\eta = 2m/m + 1 \tag{14}$$

Where m represents the strain rate sensitivity, which can be expressed as:

$$\mathrm{m} = \partial \ln \sigma / \partial \ln \dot{\varepsilon} \tag{15}$$

Based on the extreme value principle of irreversible thermodynamics and the continuum instability criterion proposed by Prasad et al. [49], an instability mapping suitable for large plastic fluids is established. Unstable parameter $\zeta(\dot{\varepsilon})$ can be given by Eq. (16):

$$\zeta(\dot{\varepsilon}) = \sigma \ln\left(\frac{m}{m+1}\right)/\sigma \ln(\dot{\varepsilon}) + m \le 0 \tag{16}$$

Unstable parameters in the formula $\zeta(\dot{\varepsilon})$ flow instability will occur when the value of is negative. Subsequently, the rheological instability map is constructed according to the changes of instability parameters, temperature and strain rate under different processing conditions. Finally, the power dissipation map and rheological instability map are superimposed to plotte the processing map.

Fig. 10 is the processing map of Cu30Cr10W and 1.0GO/0.5CeO_2-Cu30Cr10W composites under the conditions of strain 0.2 and 0.4, respectively. The shaded areas in this figure represents unstable region, and the value on the contour line represents the power dissipation efficiency. The results show that the instability region of the composite is different under different strains, indicating that the instability region of the composite shows high sensitivity to strain.

When the strain is 0.2, the instability zone of the two composites is very small and show excellent hot working properties. With the increase of strain, the instability region of the two materials increases. The instability region of Cu30Cr10W composite is mainly composed of low temperature-high strain rate (630–740 ℃, 0.09–1 s^{-1}) and high temperature-low strain rate (760–900 ℃, 0.001–0.05 s^{-1}). The instability zone of 1.0GO/0.5CeO_2-Cu30Cr10W composite exists in the region of low temperature-medium strain rate (600–700 ℃, 0.007–0.08 s^{-1}). In the process of hot working, the possibility of mechanical twinning, cavity, adiabatic shear band and cracking in the instability zone increases. Therefore, the parameters of this area should be avoided as the reference basis of hot working process. When the strain is 0.4, compared with Cu30Cr10W composite, GO/CeO_2 reinforced Cu30Cr10W composite has three areas with peak efficiency, which are considered as safe areas, as shown in Fig. 10(d) domain I~III, indicating that selecting the thermal parameters of these three areas can obtain good machinability and defect free structure.

4. Conclusion

GO/CeO_2-Cu30Cr10W composites were prepared by SPS. The isothermal compression tests were carried out on the Gleeble-1500D thermal simulation testing machine with deformation temperature of 600–900 ℃ and deformation rate of 0.001–1 s^{-1}. The conclusions can be obtained as follows:

(1) The flow stress increases with the increase of strain rate or the decrease of deformation temperature. The addition of GO and twinning mechanism increase the flow stress of Cu30Cr10W composites. The activation energy of Cu30Cr10W composite was 186.2 KJ/mol. The addition of GO and CeO_2 increased the activation energy by 8.4% and 33.1%, respectively. Based on the hyperbolic sinusoidal model, the constitutive equations of three kinds of composites were established.

(2) Amorphous carbon atoms and chromium particles formed small-size Cr_7C_3 nanoparticles at the interface between graphene and metal matrix, which contributed to the improving of interfacial bonding ability. The chromium particles were extruded into strips perpendicular to the compression direction, and the edges of tungsten particles were slightly deformed.

(3) The degree of dynamic recrystallization gradually deepened with the increase of deformation temperature, and the volume fraction of Goss texture, brass texture, copper texture and s texture decreased and changed into fiber texture.

(4) Based on the dynamic material model, the machining diagrams of Cu30Cr10W and 1.0GO/CeO_2-Cu30Cr10W composites are constructed. The introduction of GO/CeO_2 reduces the rheological instability region, which shows that GO/CeO_2 improves the heat treatment properties of the material.

CRediT authorship contribution statement

Shengli Liang: Conceptualization, Methodology, Formal analysis, Writing. **Meng Zhou:** Resources, Project administration. **Yi Zhang:** Writing – review & editing, Funding acquisition. **Shuang Liu:** Data curation, Formal analysis. **Xu Li:** Investigation. **Baohong Tian and Yong Liu:** Resources, Supervision. **Yongfeng Geng and Yijie Ban:** Formal analysis. **Yanlin Jia:** Visualization. **Alex A.Volinsky:** Writing – review & editing.

Declaration of Competing Interest

The authors declare that they have no known competing financial interests or personal relationships that could have appeared to influence the work reported in this paper.

Acknowledgments

This work was supported by the National Natural Science Foundation of China (52071134) , Natural Science Foundation of Henan Province (202300410144), The Program for Innovative Research Team in University of Henan Province (22IRTSTHN001), China Postdoctoral Science Foundation (2021T140779) and Outstanding Talents Innovation Fund of Henan Province (ZYQR201912164).

References

[1] T.J. Li, Y.Q. Wang, M. Yang, H.L. Hou, S.J. Wu, High strength and conductivity copper matrix composites reinforced by in-situ graphene through severe plastic deformation processes, J. Alloy. Compd. 851 (2021) 156703.
[2] V. Rajkovic, D. Bozic, J. Stasic, H.W. Wang, M. Jovanovic, Processing, characterization and properties of copper-based composites strengthened by low amount of alumina particles, Powder Technol. 268 (2014) 392–400.
[3] K. Dash, B.C. Ray, D. Chaira, Synthesis and characterization of copper–alumina metal matrix composite by conventional and spark plasma sintering, J. Alloy. Compd. 516 (2011) 78–84.
[4] A.M. Sadoun, A. Fathy, Experimental study on tribological properties of Cu-Al_2O_3 nanocomposite hybridized by graphene nanoplatelets, Ceram. Int. 45 (2019) 24784–24792.
[5] K.K. Gan, M.Y. Gu, The compressibility of Cu/SiCp powder prepared by high-energy ball milling, J. Mater. Process. Tech. 199 (2007) 173–177.
[6] P.K. Deshpande, R.Y. Lin, Wear resistance of WC particle reinforced copper matrix composites and the effect of porosity, Mater. Sci. Eng. A. 418 (2005) 137–145.
[7] S.R. Zhang, H.J. Kang, R.G. Li, C.L. Zou, E.Y. Guo, Z.G. Chen, T.M. Wang, Microstructure evolution, electrical conductivity and mechanical properties of dual-scale Cu5Zr/ZrB_2 particulate reinforced copper matrix composites, Mater. Sci. Eng. A. 762((2019).
[8] M. Pellizzari, G. Cipolloni, Spark plasma sintering of copper matrix composites reinforced with TiB_2 particles, Materials 13 (2020).
[9] Y.B. Fu, Q.F. Pan, Z.Q. Cao, S.F. Li, Y.Q. Huo, Strength and electrical conductivity behavior of nanoparticles reaction on new alumina dispersion-strengthened copper alloy, J. Alloy. Compd. 798 (2019) 616–621.
[10] H.Y. Li, X.H. Wang, Z.D. Hu, Y.F. Liu, Investigation of arc erosion mechanism for tin dioxide-reinforced silver-based electrical contact material under direct current, J. Electron. Mater. 49 (2020) 4730–4740.
[11] Z.F. Gao, J.X. Liang, J. Yao, Y.T. Zhao, Q. Meng, G.Y. He, H.Q. Chen, Synthesis of Ce-doped NiAl LDH/RGO composite as an efficient photocatalyst for photocatalytic degradation of ciprofloxacin, J. Environ. Chem. Eng. 9 (4) (2021) 105405.
[12] J. Phiri, P. Gane, T.C. Maloney, General overview of graphene: Production, properties and application in polymer composites, Mater. Sci. Eng. B 215 (2017) 9–28.
[13] J.Y. Wang, Z.Q. Li, G.L. Fan, H.H. Pan, Z.X. Chen, D. Zhang, Reinforcement with graphene nanosheets in aluminum matrix composites, Scr. Mater. 66 (2012) 594–597.
[14] Y.W. Zhu, S. Murali, W.W. Cai, X.S. Li, J.W. Suk, J.R. Potts, R.S. Ruoff, Graphene and Graphene Oxide: Synthesis, Properties, and Applications, Adv. Mater. 22 (2010) 3906–3924.
[15] Y. Yang, J. Dai, Y.J. Li, M.C. Jia, X.X.Y. Huang, Less defective fluorine-containing graphene with good dispersity: Preparation, characterization, and application in transparent conductive thin film, Carbon 115 (2017) 285–292.
[16] X. Gao, H.Y. Yue, E.J. Guo, H. Zhang, X.Y. Lin, L.H. Yao, B. Wang, Mechanical properties and thermal conductivity of graphene reinforced copper matrix composites, Powder Technol. 301 (2016) 601–607.
[17] Y. Lei, J.J. Ding, P.F. Yu, G.Y. He, Y.G. Chen, H.Q. Chen, Low-temperature preparation of magnetically separable Fe3O4@ZnO-RGO for high-performance removal of methylene blue in visible light, J. Alloy. Compd. 821 (2020) 153366.
[18] X.H. Zhang, Y. Zhang, B.H. Tian, Y.L. Jia, M. Fu, Y. Liu, K.X. Song, A.A. Volinsky, X. Yang, H. Sun, Graphene oxide effects on the properties of Al_2O_3-Cu/35W5Cr composite, J. Mater. Sci. Technol. 37 (2020) 185–199.
[19] Y.J. Ban, Y. Zhang, Y.L. Jia, B.H. Tian, A.A. Volinsky, X.H. Zhang, Q.F. Zhang, Y.F. Geng, Y. Liu, X. Li, Effects of Cr addition on the constitutive equation and precipitated phases of copper alloy during hot deformation, Mater. Des. 191 (2020) 108613.
[20] Y.J. Ban, Y. Zhang, B.H. Tian, K.X. Song, M. Zhou, X.H. Zhang, Y.L. Jia, X. Li, Y.F. Geng, Y. Liu, A.A. Volinsky, EBSD analysis of hot deformation behavior of Cu-Ni-Co-Si-Cr alloy, Mater. Charact. 169 (2020) 110656.
[21] Y. Hiraoka, H. Hanado, T. Inoue, Deformation behavior at room temperature of W-80vol% Cu composite, Int. J. Refract. Met. H. 22 (2004) 87–93.
[22] J. Yao, Z.F. Gao, Q. Meng, G.Y. He, H.Q. Chen, One-step synthesis of reduced graphene oxide based ceric dioxide modified with cadmium sulfide (CeO2/CdS/RGO) heterojunction with enhanced sunlight-driven photocatalytic activity, J. Colloid Interf. Sci. 594 (2021) 621–634.
[23] S.L. Liang, S. Liu, Y. Zhang, M. Zhou, B.H. Tian, Y.F. Geng, Y. Liu, Y.L. Jia, X. Li, A.A. Volinsky, Effect of in situ graphene-doped nano-CeO_2 on microstructure and electrical contact properties of Cu30Cr10W contacts, Nanotechnol. Rev. 10 (2021) 385–400.
[24] Y.X. Yan, F.Z. Nashath, S. Chen, S. Manickam, S.S. Lim, H.T. Zhao, E. Lester, T. Wu, C.H. Pang, Synthesis of graphene: Potential carbon precursors and approaches, Nanotechnol. Rev. 9 (2020) 1284–1314.

[25] Y.Q. Ning, X. Luo, H.Q. Liang, H.Z. Guo, J.L. Zhang, K. Tan, Competition between dynamic recovery and recrystallization during hot deformation for TC18 titanium alloy, Mater. Sci. Eng. A. 635 (2015) 77–85.
[26] B.J. Wang, Y. Zhang, B.H. Tian, V. Yakubov, J.C. An, A.A. Volinsky, Y. Liu, K.X. Song, L.H. Li, M. Fu, Effects of Ce and Y addition on microstructure evolution and precipitation of Cu-Mg alloy hot deformation, J. Alloy. Compd. 781 (2019) 118–130.
[27] X.H. Zhang, Y. Zhang, B.H. Tian, Y.L. Jia, Y. Liu, K.X. Song, A.A. Volinsky, Thermal deformation behavior of the Al_2O_3-Cu/(W,Cr) electrical contacts, Vacuum 164 (2019) 361–366.
[28] Y.F. Geng, X. Li, H.L. Zhou, Y. Zhang, Y.L. Jia, B.H. Tian, Y. Liu, A.A. Volinsky, X.H. Zhang, K.X. Song, G.X. Wang, L.H. Li, J.R. Hou, Effect of Ti addition on microstructure evolution and precipitation in Cu-Co-Si alloy during hot deformation, J. Alloy. Compd. 821 (2020) 153518.
[29] W.L. Cheng, Y. Bai, S.C. Ma, L.F. Wang, H.X. Wang, H. Yu, Hot deformation behavior and workability characteristic of a fine-grained Mg-8Sn-2Zn-2Al alloy with processing map, J. Mater. Sci. Technol. 35 (2019) 1198–1209.
[30] Z.Y. Ding, S.G. Jia, P.F. Zhao, M. Deng, K.X. Song, Hot deformation behavior of Cu–0.6Cr–0.03Zr alloy during compression at elevated temperatures, Mater. Sci. Eng. A. 570 (2013) 87–91.
[31] Y.F. Geng, Y. Zhang, K.X. Song, Y.L. Jia, X. Li, H.R. Stock, H.L. Zhou, B.H. Tian, Y. Liu, A.A. Volinsky, X.H. Zhang, P. Liu, X.H. Chen, Effect of Ce addition on microstructure evolution and precipitation in Cu-Co-Si-Ti alloy during hot deformation, J. Alloy. Compd. 842 (2020) 155666.
[32] B.J. Wang, Y. Zhang, B.H. Tian, J.C. An, A.A. Volinsky, H.L. Sun, Y. Liu, K.X. Song, Effects of Ce addition on the Cu-Mg-Fe alloy hot deformation behavior, Vacuum 155 (2018) 594–603.
[33] K. Chu, F. Wang, Y.B. Li, X.H. Wang, D.J. Huang, H. Zhang, Interface structure and strengthening behavior of graphene/CuCr composites, Carbon 133 (2018) 127–139.
[34] S. Anthonysamy, K. Ananthasivan, I. Kaliappan, V. Chandramouli, P.R. Vasudeva Rao, C.K. Mathews, K.T. Jacob, Gibbs energies of formation of chromium carbides, Metall. Mater. Trans. A. 27 (1996) 1919–1924.
[35] L.D. Teng, K.G. Lu, R.E. Aune, S. Seetharaman, Thermodynamic investigations of Cr_3C_2 and reassessment of the Cr-C system, Metall. Mater. Trans. A. 35 (2004) 3673–3680.
[36] F. Bittner, S. Yin, A. Kauffmann, J. Freudenberger, H. Klauß, G. Korpala, R. Kawalla, W. Schillinger, L. Schultz, Dynamic recrystallisation and precipitation behavior of high strength and highly conducting Cu-Ag-Zr-alloys, Mater. Sci. Eng. A. 597 (2014) 139–147.
[37] R. Mishnev, I. Shakhova, A. Belyakov, R. Kaibyshev, Deformation microstructures, strengthening mechanisms, and electrical conductivity in a Cu-Cr-Zr alloy, Mater. Sci. Eng. A. 629 (2015) 29–40.
[38] Y.S. W, X.Z. Qin, C.S. Wang, L.Z. Zhou, Influence of phosphorus on hot deformation microstructure of a Ni-Fe-Cr based alloy, Mater. Sci. Eng. A 768 (2019) 138454.
[39] Y.S. Wu, Z. Liu, X.Z. Qin, C.S. Wang, L.Z. Zhou, Effect of initial state on hot deformation and dynamic recrystallization of Ni-Fe based alloy GH984G for steam boiler applications, J. Alloy. Compd. 795 (2019) 370–384.
[40] Y.F. Geng, Y.J. Ban, X. Li, Y. Zhang, Y.L. Jia, B.H. Tian, M. Zhou, Y. Liu, A.A. Volinsky, K.X. Song, S.L. Tang, Excellent mechanical properties and high electrical conductivity of Cu-Co-Si-Ti alloy due to multiple strengthening, Mater. Sci. Eng. A. 821 (2021) 141639.
[41] H. Mirzadeh, Constitutive modeling and prediction of hot deformation flow stress under dynamic recrystallization conditions, Mech. Mater. 85 (2015) 66–79.
[42] C. Zener, J.H. Hollomon, Effect of strain rate upon plastic flow of steel, J. Appl. Phys. 15 (1944) 22–32.
[43] C.M. Sellars, W.J. Mctegart, On the mechanism of hot deformation, Acta Metall. 14 (1966) 1136–1138.
[44] A. Mwembela, E.B. Konopleva, H.J. McQueen, Microstructural development in Mg alloy AZ31 during hot working, Scr. Mater. 37 (1997) 1789–1795.
[45] J.J. Jonas, C.M. Sellars, W.J. Tegart, Strength and structure under hot-working conditions, Metall. Rev. 14 (1969) 1–24.
[46] B. Chen, S.F. Li, H. Imai, L. Jia, J. Umeda, M. Takahashi, K. Kondoh, Load transfer strengthening in carbon nanotubes reinforced metal matrix composites via in-situ tensile tests, Compos. Sci. Technol. 113 (2015) 1–8.
[47] Y. Gu, L.L. Hu, Effect of graphene addition on microstructure and properties of graphene/copper composite, IOP Conf. Ser: Earth. Environ. Sci. 651, 2021: 032002.
[48] F. Chen, Q.S. Mei, J.Y. Li, C.L. Li, L. Wan, G.D. Zhang, X.M. Mei, Z.H. Chen, T. Xu, Y.C. Wang, Fabrication of graphene/copper nanocomposites via in-situ delamination of graphite in copper by accumulative roll-compositing, Compos. Part. B. 216 (2021) 108850.
[49] J.T. Hou, W.B. Du, C. Parande, M. Gupta, S. Li, Significantly enhancing the strength ductility combination of Mg-9Al alloy using multi-walled carbon nanotubes, J. Alloy. Compd. 790 (2019) 974–982.